ARTICLE

Heterogeneous Nanostructures Cause Anomalous Diffusion in Lipid Monolayers

Yang Liu, Xu Zheng, Dongshi Guan, Xikai Jiang, and Guoqing Hu*

Read Online

ACCESS | Metrics & More | Article Recommendations | Supporting Information

ABSTRACT: The diffusion and mobility in biomembranes are crucial for various cell functions; however, the mechanisms involved in such processes remain ambiguous due to the complex membrane structures. Herein, we investigate how the heterogeneous nanostructures cause anomalous diffusion in dipalmitoylphosphatidylcholine (DPPC) monolayers. By identifying the existence of condensed nanodomains and clarifying their impact, our findings renew the understanding of the hydrodynamic description and the statistical feature of the diffusion in the monolayers. We find a universal characteristic of the multistage mean square displacement (MSD) with an intermediate crossover, signifying two membrane viscosities at different scales: the short-time scale describes the local fluidity and is independent of the nominal DPPC density, and the long-time scale represents the global continuous phase taking into account nanodomains and increases with DPPC density. The constant short-time viscosity reflects a dynamic equilibrium between the continuous fluid phase and the condensed nanodomains in the molecular scale. Notably, we observe an "anomalous yet Brownian" phenomenon exhibiting an unusual double-peaked displacement probability distribution (DPD), which is attributed to the net dipolar repulsive force from the heterogeneous nanodomains around the microdomains. The findings provide physical insights into the transport of membrane inclusions that underpin various biological functions and drug deliveries.

KEYWORDS: *Anomalous diffusion, Lipid membrane, Nanodomain, Anomalous yet Brownian, Heterogeneity*
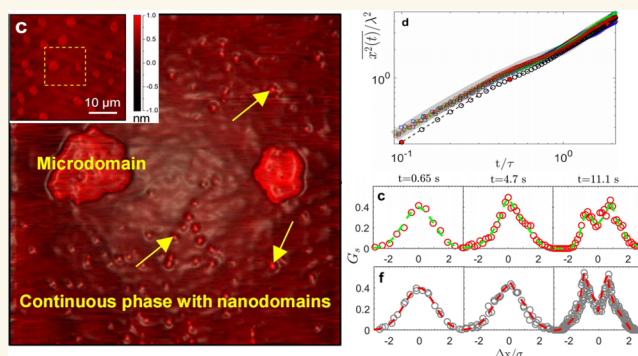
INTRODUCTION

Lipid membranes, such as cell membranes or lung surfactant membranes, are ubiquitous in biological systems. Despite their different functions, lipid membranes have a common structure—a thin film consisting of lipid and protein molecules. An early fluid-mosaic model[1] treated the live cell membrane architecture as a two-dimensional (2D) fluid matrix in which the lipids and proteins are randomly dispersed. The transport of microscale and nanoscale particles in these inherently dynamic lipid membranes is intriguing in many biological processes,[2−5] such as signal propagation, membrane trafficking, and protein sorting.[6−8] In particular, the lateral diffusion/mobility facilitated by the membrane fluidity has been found to play an important role in the dispersion of inhaled nanoparticles[9,10] and the protein-mediated transport[11,12] in pulmonary surfactant membranes and also the delivery of nanomedicine.[13,14] Thus, deciphering the diffusion in such membranes is essential for understanding many biological functions and mechanisms.

Over the past few decades, studies have shown that the fluid-mosaic model oversimplified the complex structure and dynamics of the lipid membranes.[15−19] Emerging evidence renewed the fluid-mosaic model by viewing the lipid membrane structure as "more mosaic than a fluid".[15,16] More recently, the nanostructures formed by molecular crowding or lipid−protein interaction and their impact on membrane mobility have become captivating issues.[3,5,17,19,20] Such nanostructures at lipid membranes are heterogeneous at the nanoscale, and their dynamic movement and interplay can significantly influence the membrane mobility as well as membrane biological functions.[4,21] For instance, recent experiments have revealed that the cell membranes manifest an unusual and heterogeneous flow resistance.[17,18] In particular, the crowding effect in protein-rich native cell membranes is found to be significant in the formation and
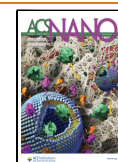
function of multiprotein complexes,[21−24] and a better understand of the protein crowding effect requires a thorough characterization of the lateral diffusion dynamics. Even in some synthetic lipid membranes for mimicking real cell membranes, heterogeneous structures due to phase separation were reported,[25−28] which caused anomalous diffusive behavior of various membrane inclusions. Here, the notion of anomalous diffusion means that the motion follows a power-law MSD (mean square displacement),[24,29,30] i.e. $\overline{x^2(t)} \approx t^\alpha$, where the exponent $\alpha > 1$ indicates a superdiffusive behavior and $\alpha < 1$ indicates a subdiffusive behavior. To date, however, how to model the diffusion and mobility in the membrane with heterogeneous nanostructures is still controversial, and the underlying nanoscale mechanism and dynamic features remain unclear.[17−21,31,32]

In fact, the hydrodynamic description of the flow resistance of diffusive inclusions in a 2D membrane has been a critical challenge.[33−35] The diffusion coefficient of membrane inclusions was initially given by Saffman and Delbrück (called the SD model).[33] By assuming that a uniform membrane at an air−water interface has a 2D viscosity η_m whose unit is Pa s m, the diffusion coefficient of a membrane inclusion in the SD model can be written as $D = k_B T/(4\pi\eta_m)\Delta(\varepsilon)$, where $\Delta(\varepsilon) = \ln(2/\varepsilon) - \gamma$ is the reduced mobility, γ is the Euler constant, $\varepsilon = \frac{r(\mu_{air} + \mu_{water})}{\eta_m}$ is the dimensionless size, r is the radius of the inclusion, and μ_{air} and μ_{water} are the viscosities of air and water, respectively. However, the SD model is a linear approximation and is only applicable to small ε values. Later, Hughes, Pailthorpe, and White (HPW) extended the SD model and applied it to describe the diffusion of larger inclusions,[34] such as condensed microdomains in synthetic lipid membranes.[25−28] Notably, the dispersed condensed domains formed by phase separation appeared not only on the micrometer scale but also on the nanometer scale in the continuous fluid phase.[19−21,36,37] The existing hydrodynamic theories, including both the SD and HPW models, fail to describe the diffusion as well as mobility of any membrane inclusions due to the presence of the heterogeneous nanodomains. Hence, it is vital to study the diffusion of membrane inclusions by considering the dynamic impact from the surrounding heterogeneous nanostructures.

Besides the hydrodynamic description, a distinct microscopic mechanism due to the heterogeneous nanostructures will cause anomalous dynamics of the diffusion on the membrane. Such anomalous dynamics signifies the nonintuitive nanoscale interactions on the membrane,[21,38] whereas no consensus has yet been reached. In contrast to the conventional studies focusing on analyzing the MSD, other statistical features, such as displacement probability distribution (DPD), have drawn increasing research attention lately.[38−41] These statistical results can provide important information such as energy barrier, interaction range, and hopping frequency in the membrane, which are urgently needed to construct a complete theoretical system to understand and model the microscopic mechanisms. Moreover, the surprising "anomalous yet Brownian" behavior, exhibiting a linear MSD but a non-Gaussian DPD, has been observed in the diffusion within heterogeneous environments.[41−44] Additional complexity comes from the temporal evolution of the DPDs,[42−44] emphasizing the rich physics involved in the interactions with the surrounding nanostructures on different time scales. Therefore, a systematic characterization of the statistical features of the diffusions is essential to understand the microscopic mechanism of the anomalous diffusions and the interactions within the membranes.

In this study, we measured the diffusion of microdomains in the monolayers of DPPC (chemical formula $C_{40}H_{80}NO_8P$, molar mass 734.05 g/mol), which is the predominant constituent of a lung surfactant film.[10,36,45] As a well-controlled 2D model membrane system, the DPPC monolayer can help disentangle the out-of-membrane effects that are difficult to avoid in live biological membranes. We identified the existence of nanoscale condensed domains surrounding the microdomains, by which we unveiled the anomalous features of the microdomain's diffusion caused by these nanodomains. Due to the confinement of the nanodomains, the measured MSD shows multiple stages and signifies two diffusion coefficients and two associated membrane viscosities at different length scales. Interestingly, we find that the short-time viscosity reflecting the local membrane fluidity remains constant, indicating a dynamic equilibrium between the continuous fluid phase and the condensed nanodomains in the molecular scale. In contrast, the long-time viscosity representing the global behavior taking into account the heterogeneous distribution of nanodomains clearly increases with DPPC density. In addition, the DPD surprisingly displays a "non-Gaussian yet Brownian" feature showing a double-peaked shape at long times, whereas the MSD remains linear. Such a DPD differs from the usual sharp-peaked DPD observed in confined diffusions on membranes,[41−43] implying the crucial role of the dipolar repulsive interaction between a microdomain and the surrounding heterogeneous nanodomains.

RESULTS

Phase Separation and Nanodomains Surrounding the Microdomains. DPPC, consisting of a polar headgroup and two long apolar alkyl chains,[46] forms a monolayer at the air−water interface. The DPPC monolayer manifests different microstructures during its phase transitions, which is usually demonstrated by an isotherm with varied molecular areas. Figure 1a shows the compression isotherm of the DPPC monolayer containing the fluorescent probe 1,2-dihexadecanoyl-sn-glycero-3-phosphoethanolamine (Texas Red-DHPE; 99.8:0.2, mol/mol) at room temperature of 20 °C. This isotherm was measured using constrained drop surfactometry (CDS, see Note 1 of the Supporting Information for details). As seen from Figure 1a, when the monolayer is compressed to moderate molecular areas approximately from 55 to 80 Å^2/molecule, within the range reported in the literature,[47,48] it exhibits a phase separation and coexistence of the condensed and continuous fluid phases, characterized by a plateau in the isotherm.[36,49] In the phase coexistence, the micrometer-sized condensed domains nucleate, appearing black, as the probe Texas Red-DHPE preferentially partitions into the continuous phase (see the two fluorescence microscopy images in Figure 1a). Additionally, as the molecular area decreases, the fractional area of microdomains increases at the cost of a decrease in the continuous phase. We observed that the microdomains show clear diffusive motions, and one trajectory is shown in Figure 1b. Here, the diffusion of microdomains was measured on the DPPC monolayers at three different surface densities, corresponding to molecular areas of 58, 68, and 81 Å^2/molecule.
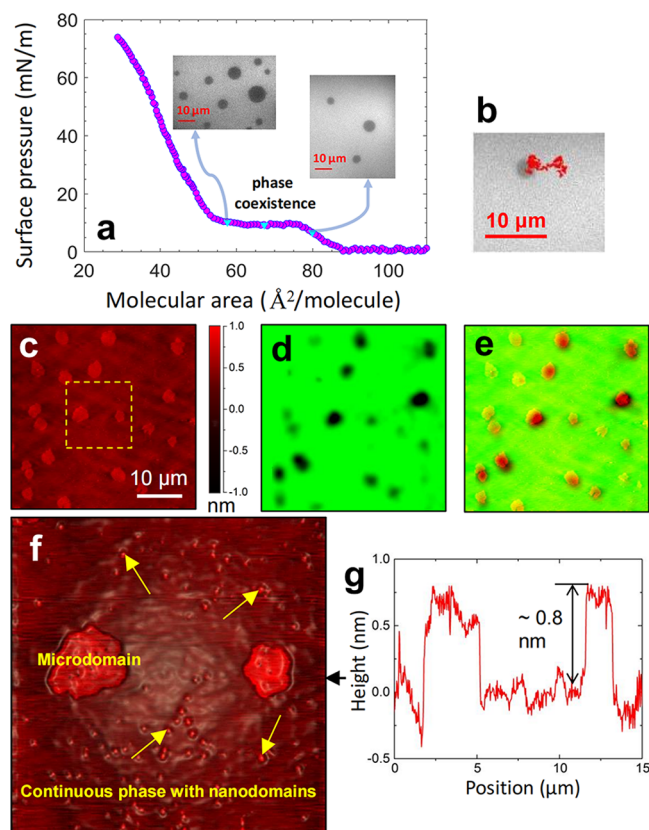
Figure 1. Characterizing the DPPC monolayer and identifying the nanodomains. (a) Compression isotherm of the monolayer composed of DPPC/Texas Red-DHPE. The three points marked in cyan are at 58, 68, and 81 Å²/molecule, representing the three DPPC densities used in this work. The insets are the fluorescence microscopy images of the condensed domains in monolayers of 81 and 58 Å²/molecule. (b) Trajectory of a diffusing microdomain. (c) AFM topographic image of the monolayer of 68 Å²/molecule on a mica surface. (d) Fluorescence microscopy image of the same monolayer on mica as (c) and in the same observation scope. (e) Overlay image of (c) and (d). (f) Enlargement of the yellow box indicated in (c). The nanodomains indicated by yellow arrows are prevalent in the continuous fluid phase. (g) Height variation along a scanning line indicated by the black arrowhead in (f).

To reveal the nanodomains on the DPPC monolayer, we used atomic force microscopy (AFM) to scan the topography of the DPPC monolayer that was transferred from the air–water interface onto a freshly peeled mica sheet (see Materials and Methods). Figure 1c shows the AFM topographic image of a transferred DPPC monolayer of 68 Å²/molecule. The bright regions are the microdomains with a larger height, whereas the dark regions are the continuous phase with a smaller height because the DPPC molecules are ordered-packed in the domains and the alkyl chains tilt at a smaller angle.[36,50] We guarantee that these domains are the original structures on the monolayer at the air–water interface rather than those formed by aggregation during drying or transferring. To confirm this, first, the transferring was not considered successful until the monolayer morphology observed on the mica surface (see the fluorescence microscopy image, Figure 1d) was similar to that on the air–water interface before transferring. Second, we compared the fluorescence image (Figure 1d) of the monolayer with its AFM image (Figure 1c) to verify that the high regions in the AFM are indeed the microdomains. This

can be confirmed in Figure 1e, which is an overlay of Figure 1c,d, displaying good accordance of the positions of the microdomains. Then, a higher resolution scan (Figure 1f) in the yellow box indicated in Figure 1c highlights the nanoscale condensed domains that cannot be observed by the fluorescence microscope due to the limit of the optical resolution. Notably, the nanodomains are prevalent in the DPPC monolayer and are nonuniformly distributed around the microdomains. In all AFM images, the domains are approximately 0.8 nm above the continuous phase, as shown in Figure 1g. Such a small height difference and the uniform height throughout the domains confirm that the domains on the mica surface are the original molecular structures of the monolayer. The size of the nanodomains is approximately 100−200 nm, and the separation between them is approximately 1−2 μm. The separation between the microdomain and the nearest nanodomains is approximately 1.5−2 μm, implying a depletion effect that could be attributed to dipolar repulsive interactions among domains.[51] Moreover, we note that the amount and size of the nanodomains slightly increase with the increasing DPPC surface density in our experiments. The prevalence of these nanodomains and the dipolar repulsive interaction are expected to cause a non-negligible impact on the microdomain's diffusion.

Distinct Diffusive Behavior at Short and Long Elapsed Times. We used a single-particle tracking technique to obtain the trajectories of individual microdomains and then calculated the time-averaged MSD of each microdomain. Figure 2a−c show the measured MSDs of the microdomains of different sizes at different surface densities. The MSDs share a similar trend: linear diffusion, i.e., MSD ≈ t, at short elapsed times, followed by a subdiffusive crossover at intermediate times t ≈ 5 s, and then the MSDs become linear again at long times. Such MSDs violate the conventional SD or HPW theories that indicate a simple linear MSD in a homogeneous membrane. The crossover demonstrates the confinement effect from the surrounding media, which has often been observed for confined diffusions in crowded and heterogeneous surroundings.[21,44,45,52−55] From Figures 2a−c, the MSD curves are shifted rightward with the increasing size of the microdomains, since larger microdomains move more slowly. Surprisingly, we find in Figure 2d that the MSDs of different microdomains with the same radius overlap together, indicating a negligible effect of the surface density of DPPC on the diffusion. Here, the surface density is a nominal value calculated by dividing the added amount of the substance of DPPC over the monolayer area. Notably, the Y-axis values of the MSDs in the crossover regime are all close to 2 μm² for the microdomains with different sizes. This result suggests that the confinement originates from the nearest nanodomains that are located ~√2 μm away from the border of the microdomain, as evidenced by our AFM scanning in Figure 1f. With the knowledge that the confinement is given by the nanodomains, the MSD results provide important information on the mesoscopic diffusive behavior, domain interaction, and spatial configuration of the nanodomains.

To highlight the occurrence of the crossover, we calculate the data of $\overline{x^2(t)}/t$. Figure 2e shows the variations of $\overline{x^2(t)}/t$ of three microdomains in the DPPC monolayer of 81 Å²/molecule (as shown in Figure 2c). We observe that each curve of $\overline{x^2(t)}/t$ manifests two horizontal plateaus connected by a sharp decline in the middle, corresponding to the two linear
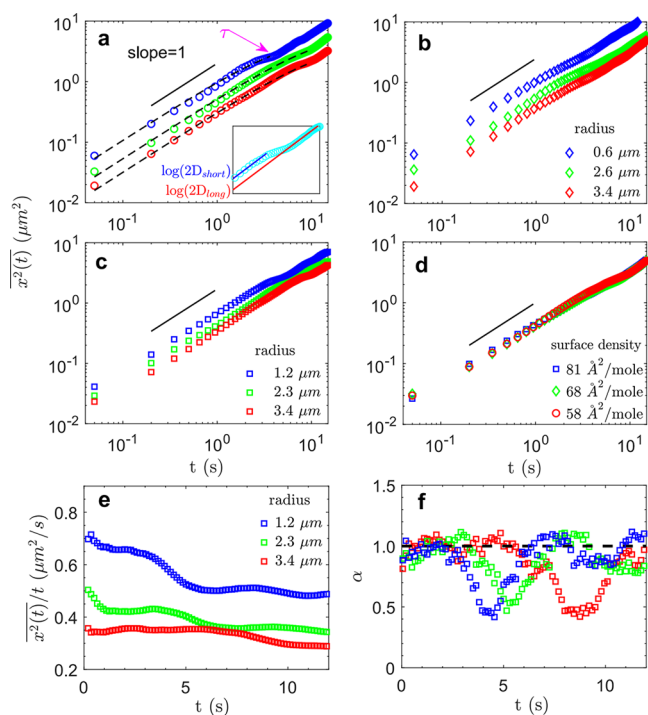
Figure 2. Multistage MSD curve with a crossover. (a) One-dimensional MSD $\overline{x^2(t)}$ as a function of the elapsed time t for microdomains of different radii on the monolayer of 58 Å²/molecule. From top to bottom, the radii of the microdomains are 1.1, 2.7, and 3.6 μm. The short black straight line shows a linear slope of MSD. The dashed lines show the fittings of the data prior to the long-time linear regime to the function $A[1 - \exp(-t/\tau)]$, with fitting parameters A and τ. The typical time scale τ is marked. (b) MSDs of the monolayer of 68 Å²/molecule. From top to bottom, the radii are 0.6, 2.6, and 3.4 μm. (c) MSDs of the monolayer of 81 Å²/molecule. From top to bottom, the radii are 1.2, 2.3, and 3.4 μm. (d) Data of three microdomains with a same radius (1.3 μm) but on monolayers with different surface densities: 81 Å²/molecule (blue); 68 Å²/molecule (green); 58 Å²/molecule (red). (e) Data of $\overline{x^2(t)}/t$ from the results in (c) for the monolayer of 81 Å²/molecule, which can better appreciate the crossover between the two linear stages manifested by the horizontal plateaus. (f) Variation of the scaling exponent $\alpha(t)$ with time, calculated from the curves in (e). For each curve in the figure, $n = 3000$ consecutive displacements are used in the statistical calculation.

stages at short and long time, respectively, and the crossover in between. We also plot the scaling exponent $\alpha(t)$ in Figure 2f by calculating the logarithmic derivative from the MSD data, which could provide information to evaluate whether the anomalous diffusion is subdiffusive or superdiffusive in addition to the crossover. For all of the experiments, the values of the exponent $\alpha(t)$ are approximately 1 at short times and decrease to approximately 0.4 during crossover, indicating a subdiffusive behavior. The smaller the microdomain, the earlier the subdiffusive crossover appears. After the crossover, the fluctuation amplitude of $\alpha(t)$ seems enlarged compared to its short-time value, showing periodic switches between subdiffusive and superdiffusive behaviors. We suspect that this fluctuation might be a signal of the nonequilibrium motion related to the time-evolving DPD at long times, as will be discussed later. It is also of interest to mention that, before the millisecond short-time stage as in the current experiment, there could be other microscopic nonlinear stages. Theoretical and numerical investigations have revealed a crossover of MSD from subdiffusion with $\alpha \approx 0.6$ around a nanosecond to $\alpha \approx 1$ around a microsecond in lipid membranes,[23,24] which was verified by a neutron spin echo spectroscopy measurement.[56]

On top of the evaluation of the MSD results, we further calculate the velocity autocorrelation function C_d, as shown in Figure 3. We can clearly observe a negative part of the autocorrelation for each curve. This negative correlation usually returns to zero when $t > 0.1$ s, as shown in Figure 3b,c. However, for the case of the lowest molecular area (Figure 3a, corresponding to the monolayer with the highest DPPC density), the negative part takes a slightly longer time to decay. This negative correlation should originate from certain forces that are against the motion of the microdomains. One possible force is due to the elastic effect of the lipid membrane,[57,58] as such a membrane is known to be inherently viscoelastic. Another source is the electric dipolar repulsive force from the surrounding condensed domains,[51] which can produce long-range repulsion and makes an important contribution to the domain−domain interaction.

The MSDs with a crossover shown in Figure 2 signify two diffusion coefficients, namely, D_{short} and D_{long}, obtained by the linear fittings of MSD vs t at short and long times, respectively, as illustrated in the inset of Figure 2a. D_{short} is always larger than D_{long}, indicating that the microdomains diffuse faster locally before they can sense confinement from neighboring nanodomains. Figure 4a,b shows the values of D_{short} and D_{long} as a function of the radius of microdomains at different surface
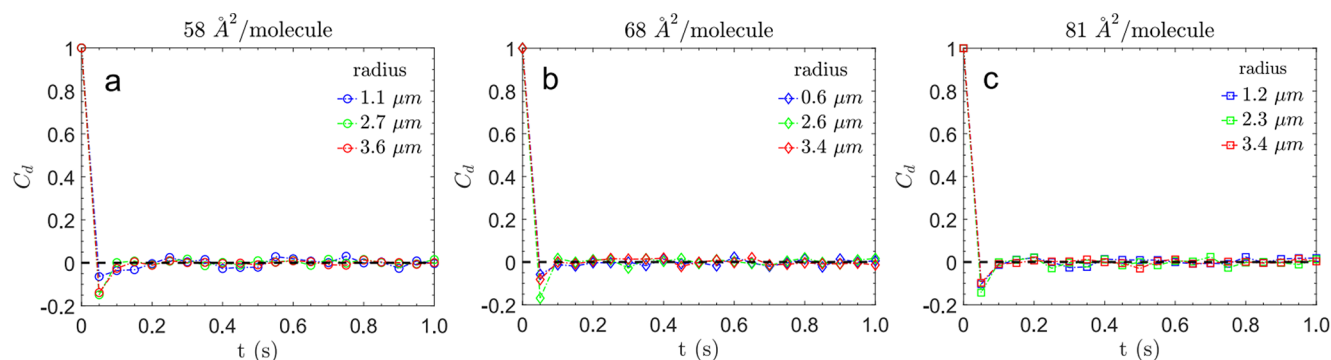

Figure 3. Negative correlation of autocorrelation functions. (a−c) Data for a DPPC monolayer with molecular area, 58, 68, and 81 Å²/molecule, respectively. The colors represent different microdomain radii, as noted in the figures.
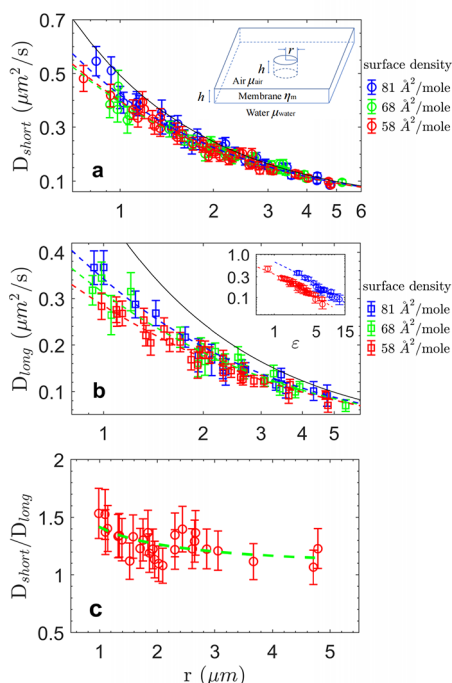
Figure 4. Diffusion coefficients at short and long times. (a) D_{short} vs r (radius of microdomains) on monolayers with different surface densities: 81 Å²/molecule (blue); 68 Å²/molecule (green); 58 Å²/molecule (red). The error bars are the standard deviations from the linear fittings of MSD vs t at short times. The inset picture shows that a cylindrical inclusion diffuses within a membrane at the air−water interface. (b) D_{long} vs r. The logarithmic inset shows D_{long} vs ε: at 81 Å²/molecule (blue) and at 58 Å²/molecule (red). In both (a) and (b), dashed lines are fittings of D_{short} and D_{long} to the HPW model. The black solid lines are the asymptotic solution of the HPW model for $\varepsilon = \infty$. (c) D_{short}/D_{long} vs r at 58 Å²/molecule. The green dashed line in (c) is the prediction of the HPW model using η_{local} and η_{global} from the fittings. For each point in this figure, n = 3000 consecutive displacements are involved in the calculation of its mean value. Error bars are calculated based on the standard deviation of the data.

densities. Both D_{short} and D_{long} decrease nonlinearly with increasing size, and we found that they can be fitted to the HPW model (dashed lines) separately by introducing a 2D membrane viscosity η_m. Even though the hydrodynamic theory of HPW fails to describe the complete diffusion, it applies to the short-time and long-time stages, respectively. Correspondingly, two membrane viscosities are needed to describe the monolayer: η_{local} that is used to fit D_{short} to the HPW model and η_{global} for D_{long}. The solution of the diffusion coefficient in the HPW model can be written as[33,34] $D = k_B T/(4\pi\eta_m)\Delta(\varepsilon)$, where $\Delta(\varepsilon)$ is the reduced mobility. As directly solving the HPW model involves a complicated computation, an explicit equation of $\Delta(\varepsilon)$[59] is mathematically provided as a high-precision approximation of the HPW solution

$$\Delta(\varepsilon) = \left[\ln\left(\frac{2}{\varepsilon}\right) - \gamma + \frac{4\varepsilon}{\pi} - \left(\frac{\varepsilon^2}{2}\right)\ln\left(\frac{2}{\varepsilon}\right) \right]$$
$$\times \left[1 - \left(\frac{\varepsilon^3}{\pi}\right)\ln\left(\frac{2}{\varepsilon}\right) + c_1\varepsilon^{b_1}/(1 + c_2\varepsilon^{b_2}) \right]^{-1} \quad (1)$$

where γ = 0.5772 is the Euler constant and the parameters are c_1 = 0.7376, b_1 = 2.7482, c_2 = 0.5212, and b_2 = 0.5147, respectively. The black solid lines in Figure 4a,b are the asymptotic solutions of the HPW model for infinitely large dimensionless size ε:
$D(\varepsilon \to \infty) = = \frac{k_B T}{4\pi\eta_m} \times \frac{\pi}{2\varepsilon} = k_B T/8r(\mu_{air} + \mu_{water})$, which is independent of η_m. The SD model fails to fit D_{short} and D_{long}, because our ε values range from approximately 0.8 to 12 (see inset of Figure 4b), far above the scope $\varepsilon < 0.1$ where the SD model should apply. More details of the comparison of the HPW and SD models are shown in Note 2 and Supplementary Figure S2 of the Supporting Information.

In Figure 4a, we show all the data of the diffusion coefficients D_{short} at short times on DPPC monolayers with different surface densities. Interestingly, we notice that D_{short} does not obviously change with the nominal surface density. This is consistent with Figure 2d, in which the short-time MSDs are independent of the nominal surface densities. Figures 4a and 2d imply that in our experiments increasing the DPPC amount does not noticeably change the molecular density in the continuous phase of the membrane, which is supported by the plateau in the compression isotherm (Figure 1a), indicating that the surface pressure of the membrane also does not vary with surface density. Figure 4a also shows that the data of D_{short} for large sizes are located near the asymptotic solution (black solid line) for $\varepsilon \to \infty$ based on the HWP model. In contrast, D_{long} in Figure 4b deviates significantly from the asymptotic solid line, indicating that a larger membrane viscosity η_{global} is required to fit the data. Note that D_{long} decreases as the surface density increases (inset of Figure 4b), particularly for small microdomain sizes. Table 1

Table 1. Membrane Viscosities η_{local} and η_{global} at Different Surface Densities

	molecular area (Å²/molecule)		
	58	68	81
$\eta_{local} \times 10^{-10}$ (Pa s m)	1.8 ± 0.7	2.0 ± 0.8	1.2 ± 0.9
$\eta_{global} \times 10^{-10}$ (Pa s m)	7.7 ± 1.0	5.7 ± 1.4	4.2 ± 1.2

gives the values of the membrane viscosities used to fit D_{short}, D_{long}, η_{local}, and η_{global}. Based on the above discussion of the MSDs, we deem that η_{local} represents the surface viscosity of the local continuous phase, whereas η_{global} represents the global membrane viscosity taking into account of nanodomains. As a result, η_{local} is always smaller than η_{global} at each surface density. Moreover, the membrane viscosity of the local continuous phase η_{local}, with an average value of 1.7×10^{-10} Pa s m, does not change clearly with the nominal surface density within the experimental uncertainties. This constant short-time viscosity reflects a dynamic equilibrium between the continuous fluid phase and the condensed nanodomains on the molecular scale. In comparison, η_{global} increases as the surface density increases. This tendency can also be seen by the variation of D_{long} vs ε displayed in the logarithmic inset of Figure 4b, where D_{long} at 81 Å²/molecule is shifted to the right relative to that at 58 Å²/molecule. The increasing trend of η_{global} with the surface density can be explained by AFM scanning (Figure 1), in which we found that the size and number of nanodomains increase with increasing surface density of the monolayer. The above results indicate an intrinsic feature of the DPPC monolayer in its coexistence phase: added DPPC molecules

would aggregate to the condensed nanodomains rather than disperse in the continuous fluid phase. Using the average value $\overline{\eta_{global}} = 5.9 \times 10^{-10}$ Pa s m in Table 1, we estimate the ratio of the viscous effect of the membrane to the aqueous phase $\overline{\eta_{global}}/h\mu_{water}$ to be approximately 250, where $h = 2.4$ nm is the thickness of the DPPC monolayer. This enormous ratio implies a significant effect of the membrane viscosity that dominates the mobility of an embedded particle with sizes up to 250 times the membrane thickness.

Figure 4c plots the ratio D_{short}/D_{long} as a function of the radius of microdomains at 58 Å^2/molecule. The ratio D_{short}/D_{long} is always larger than 1 and decreases as the microdomain's radius increases, which can be described by the HPW model calculated using η_{local} and η_{global} obtained from the above, respectively. The trend of D_{short}/D_{long} decreasing with the radius indicates that the subdiffusion stage is more obvious for small microdomains. Similar phenomena were also observed in polymer systems when the size of the diffusing particle was smaller so that it approached the polymer mesh size.[44,60]

Universal Scaling of the MSD Based on an Energy Barrier Model. The anomalous diffusive behaviors shown above, combined with the heterogeneous membrane nanostructure scanned by AFM, provide valuable physical insights into the spatial distribution of the nanodomains and the interaction between a microdomain and surrounding nanodomains. From a view of the energy landscape of the membrane, the spatial distribution of nanodomains can be analogous to a distribution of energy barriers that influence the motion of microdomains[61] (Figure 5a). The microdomain can be approximated as diffusing under an energy landscape $V(x)$ by envisaging the nanodomains as the energy maximums with a period of λ. We thus establish a model to help understand the diffusion mechanism affected by these nanodomains.

The domain−domain interaction is complicated, which contains various physical sources such as electrostatic force, curvature effect, long-range attractive effect, hydrodynamic force, etc. Here, we show that the dipolar repulsive force is the major contribution and estimate this force between different domains (Supplementary Note 3 in the Supporting Information). The dipolar repulsive force between two neighboring microdomains can be approximated using $|\overrightarrow{F_{MM}}| = \frac{3\pi\xi^2 R^4}{4\varepsilon_0\varepsilon^*}\frac{1}{d^4}$, where $\varepsilon^* = \frac{\varepsilon_D^2(\varepsilon_w + \varepsilon_a)}{2\varepsilon_w\varepsilon_a}$, by treating them as two point dipoles because their distance is relatively large,[51] with d and R being the center−center distance and their radius respectively, ξ is the excess dipole density of the condensed domains with respect to the continuous fluid phase, and ε_0, ε_a, ε_w, and ε_D are the dielectric permittivities of vacuum, air, water and DPPC, respectively. The force between a microdomain and one nearby nanodomain can be obtained by integrating the force over the microdomain:
$|\overrightarrow{F_{MN}}| = \frac{3\xi^2 a_{nano}}{4\pi\varepsilon_0\varepsilon^*}\int_0^{2\pi}\int_0^R \frac{r_1(\lambda + R - r_1\cos\theta)}{[r_1^2 + (R+\lambda)^2 - 2r_1(R+\lambda)\cos\theta]^{5/2}}dr_1\,d\theta$ (Figure 5a), with a_{nano} as the area of the nanodomain. The result shows that the dipolar repulsive force between the microdomain and one of its nearest nanodomains is usually 2 times larger than the force between two neighboring microdomains. Thus, the confinement effect due to the dipolar repulsive force from the nearest surrounding nanodomains on the microdomain's diffusion is rather local, and it is rational to neglect
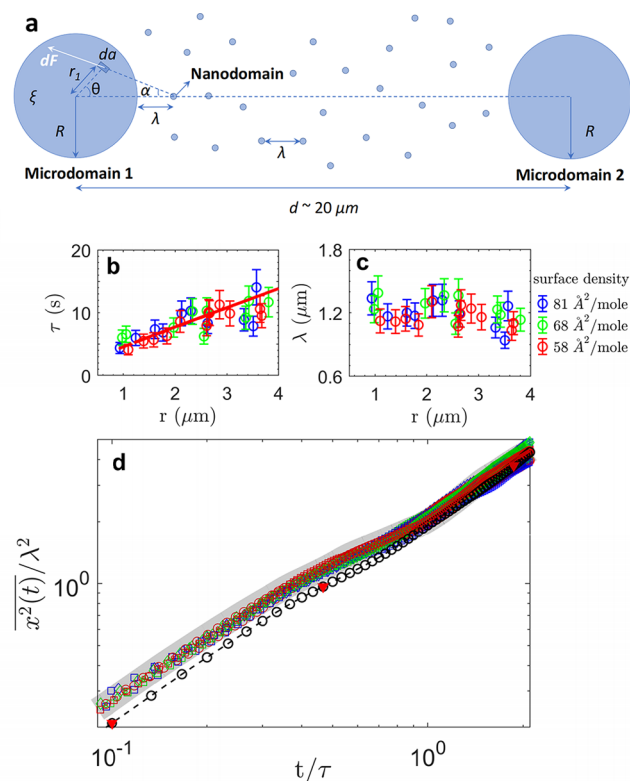

Figure 5. Spatial distribution of nanodomains and the universal scaling of the dimensionless MSDs based on an energy barrier model. (a) Schematic diagram of the monolayer structure. Microdomains 1 and 2 are separated by d. The separations between a microdomain and a nanodomain and between nanodomains are both λ. The motion of the microdomain is analogous to diffusion over a periodic energy landscape $V(x) = V_0\cos\left(\frac{2\pi x}{\lambda}\right)$ by treating nanodomains as energy maximums with a period of λ. (b) τ vs r (radius of microdomains) on monolayers with different surface densities: 81 Å^2/molecule (blue); 68 Å^2/molecule (green); 58 Å^2/molecule (red). The error bars are the standard deviations when fitting MSD vs t prior to the long-time linear stage. The red line shows τ calculated by the equation $\tau = \frac{2\overline{\lambda}^2}{D_{long}} = 2\overline{\lambda}^2/k_B T \times (4\pi\overline{\eta_{global}})/\Delta_{HPW}\left(\frac{r(\mu_{air} + \mu_{water})}{\overline{\eta_{global}}}\right)$, with $\overline{\eta_{global}} = 5.9 \times 10^{-10}$ Pa s m from Table 1, and $\overline{\lambda} = 1.2$ μm taken from (c). (c) λ vs r. (d) Dimensionless scaling of $\overline{x^2(t)}/\lambda^2$ vs t/τ. This graph contains all the experimental data (shown in colorful dots here) that appear in Figure 2a−d. Their universal trend is highlighted by a gray band in (d). The empty black circles are from our simulation.

the effects from the neighboring microdomains. It is necessary to mention another local confinement effect due to the viscoelasticity of the DPPC membrane. The elastic force from the membrane is against the microdomain's motion, causing the negative correlation shown in Figure 3 as well. However, the membrane elasticity has been found to be important only at high-frequency dynamics,[58] according to the measured elastic modulus of lipid membranes. Hereafter, when we discuss the confinement taking effect in a few seconds or even longer, we consider the dipolar repulsive force as the dominant effect.

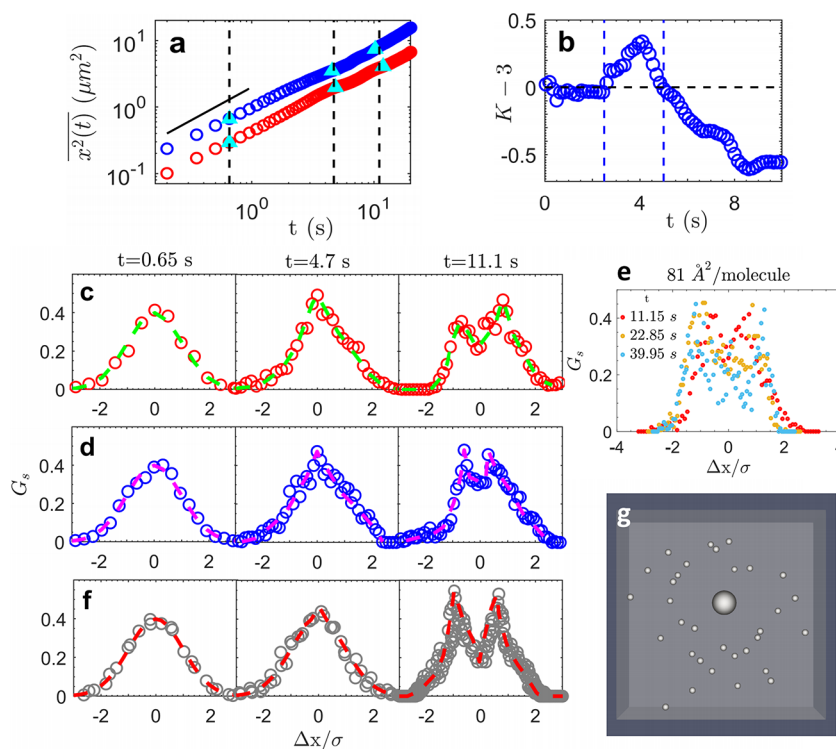We further use a mean-first-passage-time (MFPT) approach[61,62] to describe the diffusion process surrounded by

Figure 6. Temporal-evolved DPD and the double-peak feature at long times. (a) MSDs $\overline{x^2(t)}$ vs t for microdomains with different radii, $r = 1.0\ \mu$m (blue) and $r = 2.3\ \mu$m (red), on the monolayer of 81 Å^2/molecule. (b) Excess kurtosis $K - 3$ vs t for the data plotted by the blue curve in (a). (c) Normalized DPD G_s vs $\Delta x/\sigma$ (the normalized displacement) for the data plotted by the red curve in (a) at three representative elapsed times, marked by cyan triangles in (a). In the leftmost panel, the dashed line shows the standard Gaussian distribution. In the remaining two panels, the dashed lines are guidelines for the experimental data. (d) G_s vs $\Delta x/\sigma$ for the data plotted by the blue curve in (a) at three representative elapsed times. (e) Three double-peaked DPDs at $t = 11.15$ s, $t = 22.85$ s, and $t = 39.95$ s, respectively, showing a slow broadening tendency of the separation between the two peaks. (f) G_s vs $\Delta x/\sigma$ from the simulation at three representative normalized elapsed times (t/τ) that are marked by the red triangles in Figure 5d. (g) Snapshot of particles at an instant time during the simulation. In (c) and (d), three independent measurements containing $n = 3000$ displacements each are used to obtain the DPD. In (f), over 150000 displacements from simulation are used to calculate the DPD for each case.

the energy barrier from the nanodomains. This MFPT approach quantifies the typical time that the microdomain needs to diffuse a distance λ from the origin, which also indicates the characteristic time of the crossover of the measured MSDs, i.e., τ, as the diffusion has been confined by the energy barrier. Based on this crossover, the MFPT approach can theoretically establish a connection between the local short-time diffusion confined by the barrier and the global long-time diffusion as[61,62]

$$D_{\text{long}} = \frac{1}{2}\frac{z}{L}\frac{D_{\text{short}}}{R_\lambda} \tag{2}$$

where

$$R_\lambda = \langle e^{V(x)/k_BT}\rangle_\lambda \langle e^{-V(x)/k_BT}\rangle_\lambda \tag{3}$$

Here, the parameter R_λ is determined from the energy landscape $V(x)$, $\langle...\rangle_\lambda$ denotes calculating the average over a period of λ, L represents the dimensionality, and z is the number of nearest nanodomains for a microdomain. Considering the one-dimensional diffusion of the microdomain, $L = 1$ and $z = 2$. The MFPT for the microdomain to diffuse a distance λ from the origin is given by[59,61]

$$\tau = \frac{\lambda^2}{D_{\text{short}}}R_\lambda \tag{4}$$

where τ is also the characteristic time of the crossover of the MSDs.[55] We obtain the value of τ by fitting MSD vs t prior to the long-time linear stage to the equation MSD $= A(1 - e^{-t/\tau})$, where A and τ are two fitting parameters. The fits have been shown by the dashed lines in Figure 2a, and the values of τ are plotted as a function of the radius of microdomains in Figure 5b. Figure 5b shows that τ increases with increasing radius r of the microdomains because larger microdomains move more slowly and spend a longer time dwelling among the nanodomains.

Substituting the value of τ into eqs 2 and 4, the spatial separation between domains λ can be calculated using $\lambda^2 = \tau D_{\text{long}}$, with D_{long} being known from Figure 4b, and the λ values are shown in Figure 5c. We see that the separation between domains λ does not obviously change with the microdomain's size or the surface density of the monolayer. The averaged λ is approximately 1.2 μm, in good agreement with the separation between nanodomains shown by AFM scanning (Figure 1f). The red line in Figure 5b plots the theoretically calculated values of τ using

$$\tau = \frac{2\overline{\lambda}^2}{D_{\text{long}}} = 2\overline{\lambda}^2/k_BT \times (4\pi\overline{\eta_{\text{global}}})/\Delta_{\text{HPW}}\left(\frac{r(\mu_{\text{air}} + \mu_{\text{water}})}{\overline{\eta_{\text{global}}}}\right), \text{ with}$$

$\overline{\eta_{\text{global}}} = 5.9 \times 10^{-10}$ Pa s m taken from Table 1 and $\overline{\lambda} = 1.2$ μm. This red line describes the increasing trend of τ very well,

which results from the little varied λ over different domain sizes and a decreasing D_{long} with the sizes.

Knowing the typical scales τ and λ characterizing the confined diffusion, we are able to establish a dimensionless scaling law between $\overline{x^2(t)}/\lambda^2$ and t/τ. Figure 5d shows that all the dimensionless experimental curves display the same tendency highlighted by a gray band, particularly at short elapsed times, which suggests that the diffusion of microdomains with different sizes actually obeys the same scaling law under this theory.

In addition, the model above can help estimate the energy barrier E_b, which is closely related to the ratio $R_\lambda = D_{\text{short}}/D_{\text{long}}$ (eqs 2 and 3). Although it is difficult to know the explicit expression of $V(x)$, we can approximately estimate the energy barrier E_b based on eqs 2 and 3 by assuming a small value of E_b. For instance, the energy landscape near the microdomain is treated as the cosinusoidal function $V(x) = V_0 \cos\left(\frac{2\pi x}{\lambda}\right)$, where $V_0 = \frac{E_b}{2}$. We substitute $V(x)$ into eqs 2 and 3 and obtain

$$\frac{D_{\text{short}}}{D_{\text{long}}} = R_\lambda = \langle e^{E_b/2 \cos(\frac{2\pi x}{\lambda})/k_B T} \rangle_\lambda \langle e^{-E_b/2 \cos(\frac{2\pi x}{\lambda})/k_B T} \rangle_\lambda$$

$$= \frac{1}{\lambda^2} \int_0^\lambda e^{E_b/2 \cos(\frac{2\pi x}{\lambda})/k_B T} \, dx \int_0^\lambda e^{-E_b/2 \cos(\frac{2\pi x}{\lambda})/k_B T} \, dx$$

$$(5)$$

According to Figure 4c, the average value of $R_\lambda = D_{\text{short}}/D_{\text{long}}$ is 1.27. Substituting this value into Figure 5, we deduce $E_b/k_B T = 1.4$, which is a relatively small energy barrier generated by the nanodomains. As seen from Figure 4c, $R_\lambda = D_{\text{short}}/D_{\text{long}}$ decreases as the size of the microdomains increases. Therefore, based on eq 5, E_b should be larger for smaller microdomains, implying a relatively strong confinement from the nanodomains for smaller microdomains.

We notice that the above energy barrier model using the MFPT approach usually works in a static energy landscape. In the present experiments, the energy landscape around a microdomain mainly fluctuates with the dynamic rearrangement of the surrounding nanodomains. When the microdomain still gets jammed by the nanodomains and the rearrangement of the nanodomains is not fast, applying the energy barrier model at short times can help estimate the typical confinement time τ from the crossover. The nanodomains are prevalent on the membrane having a high density. If one nanodomain is pushed away from its original position, another nanodomain will move to that region by other nanodomains' repulsion so that the membrane system maintains a low energy state. Even at long times, the potential distribution V of the energy landscape should maintain a periodic fluctuation with a similar wavelength λ in a time-average view. Nonetheless, we underline that the energy landscape of the membrane is dynamic and complicated, and the domains' motion is nonequilibrium. A theoretical approach to deal with the nonequilibrium energy barrier can refer to the method based on the stochastic nonlinear Langevin equation.[63,64] Using eqs 2−5 is just an approximation to estimate the confinement time characterizing the crossover and the mean wavelength representing the time-average energy landscape. Precisely characterizing the energy landscape and its key parameters still needs further investigation.

Temporal-eEvolved DPD and Double-Peaked Feature. It was commonly believed that the diffusion with confinement shows a non-Gaussian DPD with a sharp peak at the center and narrower waists at two sides, as observed in the diffusions of inclusions in crowded biological membranes.[20,21,42,43] However, here, we obtain temporal-evolved DPDs and find a surprising double-peaked DPD even at long elapsed times, which was once reported to occur in man-made active systems[66] but has been considered as being uncommon in a crowded passive system such as the present one. Figure 6c shows the temporal evolution of the measured DPDs (red) of a microdomain with radius $r = 2.3\ \mu m$ at three different elapsed times $t = 0.65, 4.7, 11.1$ s, respectively. Figure 6d gives the DPDs (blue) of another microdomain with radius $r = 1.0\ \mu m$ at almost the same times, which manifests similar shapes of DPD respectively compared with Figure 6c. Their corresponding MSDs are displayed in Figure 6a with the same colors, respectively, and the three times are marked by cyan triangles. These three times are located respectively in the short-time stage, crossover, and long-time stage; thus, the three typical shapes of the DPDs in Figure 6c,d represent distinct diffusive dynamics in different stages.

The DPD at the short elapsed time is well described by a standard Gaussian distribution, $G_s = \frac{1}{\sqrt{2\pi}} \exp\left(-\frac{\Delta x^2}{2\sigma^2}\right)$, where σ is the standard deviation of the displacement. At this early stage, the microdomain can diffuse almost freely in the continuous phase. In the crossover stage with subdiffusive MSD, the DPD deviates from the standard Gaussian distribution and generates a sharp peak at $\frac{\Delta x}{\sigma} = 0$ and has a relatively narrow waist, which results from the confinement of the nanodomains nearby. Such a sharp peak non-Gaussian DPD has been commonly observed in crowded biomembranes[21,22] where the volume excluded effect is important, or in confined diffusion close to boundaries.[30,61,65] At long elapsed times, surprisingly, a double-peaked DPD appears. We emphasize that this double-peaked DPD does appear even when the MSD recovers to linear in the early long-time regime $t \approx 10$ s, which clearly displays an "anomalous yet Brownian" feature.[42] Obviously, the double-peaked DPDs differ from previously reported non-Gaussian DPDs that contain a central sharp peak or heavy tails.[2,41−44,67] In our case, the double-peaked feature and the DPD's temporal evolution indicate the nonequilibrium dynamics of the lateral diffusion on the membrane and provide important physical information about the interaction between the microdomain and surrounding nanodomains. The double-peaked DPD can be even observed at a much longer elapsed time. As shown in Figure 6e, such a double-peaked DPD still exists when $t \approx 40$ s. The three DPDs display similar shapes from roughly $t \approx 10$ s to $t \approx 40$ s, but the separation between the two peaks increases slowly with a speed of about 0.1 μm/s. Interestingly, within our measurement range of elapsed time of about 100 s, we do not see the recovery of the DPD to Gaussian.

The excess kurtosis, defined as $K - 3 = \frac{\langle(\Delta x)\rangle^4}{\langle(\Delta x)\rangle^2} - 3$, is a good measure of non-Gaussian DPDs, which is zero for a Gaussian or a normal distribution.[43,44] A positive excess kurtosis is obtained when the DPD shows a narrower peak at the center or fatter tails at two sides than the Gaussian distribution, whereas a negative excess kurtosis occurs in a DPD with a broader peak or lighter tails. Figure 6b shows the excess kurtosis as a function of the elapsed time for the data of the blue curve (microdomain $r = 1.0\ \mu m$) in Figure 6a. Three stages are observed in this excess kurtosis as well,

corresponding to three DPDs with different shapes shown in Figure 6c: the excess kurtosis stays close to zero until $t \approx 2.5$ s, subsequently becomes positive, and then reverses to negative upon $t \approx 5$ s. Similar evolutions of the excess kurtosis are observed for other microdomains.

We argue that this unique double-peaked DPD should be closely related to the negative correlations of the microdomain's motion in a confining environment, as have been shown in Figure 3. The negative correlation can be understood as repulsive forces or reflecting a potential barrier exerting on the microdomain that is against the motion of the microdomain. Such repulsive forces in our experiments can have two origins: the dipolar repulsive force from nearby nanodomains and the elastic force from the viscoelastic DPPC membrane. As the elastic force from the membrane is not important in low-frequency dynamics, the repulsive force is mainly attributed to the dipolar force from the surrounding nanodomains, as discussed and calculated above. We notice that a recent theoretical work[68] has shed light on understanding the correlations in motion confined by a potential barrier, in which the authors concluded that negative correlations lead to a depletion of diffusive particles from a static repulsive barrier. In our experiments, the rearrangement of the nanodomains is dynamic in the DPPC monolayer, which gives rise to the uneven distribution of the nanodomains around a microdomain (refer to the AFM image in Figure 1f). Such unevenly distributed nanodomains can result in a net dipolar repulsive force that pushes the microdomain to the side with fewer nanodomains, which forms the fluctuating potential barrier leading to the negative correlation. The dynamic rearrangement and the uneven confinement from the nanodomains cause the deviation of the DPD's peak: i.e., the peak is pushed away from the symmetric position in the middle to both sides. It is intriguing to see that the double-peaked DPD is still evolving at long times (Figure 6e), which clearly indicates the situation is nonequilibrium. We suspect that such a non-Gaussian double-peaked DPD will never return to Gaussian as long as the nanodomains keep rearranging in a nonequilibrium environment. At an infinitely long time, the DPD may become a uniform distribution within a separation between two nearby repulsive energy barriers.[68]

Computational Modeling of the DPPC Monolayer with the Nanodomains. We performed Brownian dynamics simulations containing hydrodynamic interactions to model the experimental system by including the dipolar repulsive interaction between the microdomain and nanodomains. The validation and details of the simulation are illustrated in Supplementary Note 4 and Supplementary Figure S4 in the Supporting Information. We monitored the diffusion of a large hard spherical particle (representing the microdomain) surrounded by small hard spherical particles (representing nanodomains) in a viscous fluid. The simulation system was a box of 60 (dimensionless unit) in both the x and y directions. The lateral dimensions of the box were much larger than the height, which was 18 to match the thin DPPC monolayer. The hydrodynamic effect, random Brownian motion, and dipolar repulsive force between particles were all considered. Supplementary Figure S3 shows the initial configuration of the particles in the system. Although the simulation approximates the real experiments by assuming spherical particles for the micro-/nanodomains, it can still capture the key factors of the dynamics in the experiments. Figure 6f shows the DPDs of the simulation at three different elapsed times,

which are marked by red triangles in the corresponding MSD plotted by empty black circles in Figure 5d. The simulated DPDs exhibit shapes and temporal evolution similar to those in the experiments. In addition, the MSDs also have the same trend as those in the experiments: a linear regime at short elapsed times followed by a subdiffusive crossover and a linear regime again at long elapsed times. A snapshot of the diffusive particles at an instant of time during the simulation (see Figure 6g) confirms that the nanodomains diffuse dynamically around the microdomain and may become unevenly distributed. This result supports our aforementioned explanation that the dynamic rearrangement of the nanodomains causes a net repulsive force on the microdomain to generate the double-peaked DPDs at long elapsed times. By suitable modeling of the dipolar repulsive force between domains and the multistage hydrodynamic viscosity of the membrane, our simulation reproduces all of the diffusive features and provides a complete description for the diffusive dynamics in the DPPC monolayer.

DISCUSSION

In the above sections, we summarize the crossover connecting two linear stages of the MSD on a time scale approximately from milliseconds to 10 s and the non-Gaussian behaviors characterized by the temporal evolution of the DPD. This result, in combination with the existing results about another crossover on a nanosecond scale,[23,24,56] might help establish a more comprehensive picture regarding the diffusive dynamics in lipid membranes based on MSD. The microscopic crossover, following approximately $t^{0.6}$ occurring from nano-seconds to sub-microseconds, is determined by the lipid molecular trapping and the crowding effect from the embedded macromolecules.[23,24,56] The present experiment shows a mesoscopic crossover bridging the continuous-phase diffusion and the confinement from condensed-phase nano-domains. At longer times, a linear MSD should be expected, whereas we suspect that the non-Gaussian double-peaked DPD will always be a prominent feature. Besides, we clarify the applicable scope of the SD model and highlight that the HWP model can describe respectively the short-time and long-time viscosities of a 2D fluid membrane with a molecular thickness.

The result here not only reveals the non-Gaussian double-peaked DPD in DPPC monolayers but also depicts its origin in such a nonequilibrium system. Recent progress in the study of the non-Gaussianity of the diffusive dynamics is a theoretical work considering the "diffusing diffusivity" in a viscoelastic system,[69] which is in line with our observation of the periodic-like fluctuation of the exponent $\alpha(t)$ of MSD. An obstacle causing an excluded volume effect has been frequently discussed as well, which is known to form a narrow peak DPD.[65,70] The heterogeneity of the spatial distribution of the obstacles was also tested, and the result indicated a higher non-Gaussianity by using denser heterogeneous structures.[71] Our experiment does not show increased non-Gaussianity by increasing the nominal DPPC molecular density. The plateau in the compression isotherm (Figure 1a) of the phase coexistence implies that increasing the DPPC amount does not change the molecular density in the continuous phase, and the additional DPPC molecules should be adsorbed to the condensed phase domains due to mass conservation.

It is also necessary to emphasize that the membrane in our experiment is purely DPPC and protein-free. The diffusive dynamics only represents the contribution from lipid molecules and is different from that of protein-rich

membranes. The crowding effect of proteins has been a research focus,[21,22] showing the critical roles of the macromolecular complexity and spatiotemporal membrane heterogeneity in determining the stochastic nature of the lateral diffusion. Despite the current experimental system using a pure DPPC lipid monolayer is protein-free, it can still serve to clarify the membrane fluidity and distinguish the contribution of the heterogeneous nanodomains and the continuous phase that are prevalent in many lipid membranes.

On top of the issues above, the surface curvature elasticity has been found to be important in cell membranes.[2,72] The surface curvature will appear and induce significant curvature elasticity when the inclusion has larger thickness than the membrane or imposes a nonzero contact angle due to different hydrophobicities.[72] However, we believe that the surface curvature effect is trivial in our 2D monolayer system produced on flat air−liquid interfaces. First, in our experiment, the thickness of the condensed nanodomain is only 0.8 nm thicker than the surrounding LE phase (as shown in Figure 1g). This protrusion thus introduces a nanoscale surface curvature radius on the edge of the nanodomain, which is unlikely to affect much the domain−domain interaction with a domain separation larger than 1 μm. Second, if the domain can locally tilt the membrane, imposing a contact angle, the surface curvature elasticity will become long range. In such cases, according to Goulian's theory,[72] the elastic interaction potential $V_e(d)$ between two domains with separation d is approximately: $V_e(d) \approx \kappa(Rh)^2/d^4$, where κ is the bending rigidity and R and h are the radius and thickness of the domain, respectively. Even for a microdomain, this potential will become trivial when the domain separation $d > 100$ nm, which is much smaller than the nanodomain separation in our experiments. Furthermore, the elastic potential $V_e(d)$ decays with d^4, which is faster than the dipolar repulsive potential decaying with d^3. As a result, we think that the dipolar repulsive force is more significant than other elastic effects when the heterogeneous nanodomains emerge.

CONCLUSIONS

In this work, we identify the existence and structure of the condensed nanodomains on DPPC monolayers and find that these nanodomains significantly affect the hydrodynamic mobility and the statistical feature of membrane diffusion, which are different from the existing theories considering the membrane as homogeneous. We decipher the contribution of these heterogeneous nanostructures on membrane mobility and diffusion by revealing the diffusive dynamics of the embedded microdomains in the local continuous phase and confined due to the nanodomain−microdomain interactions. The diffusion can be divided into multiple stages: short-time linear motion, then confined diffusion, and finally "anomalous yet Brownian" behavior that shows a linear MSD but an unusual double-peaked DPD. Thus, two membrane viscosities are needed to describe the hydrodynamic mobility of the microdomains: the short-time viscosity describes the local continuous fluid phase, which is found to be independent of the nominal surface density of DPPC, and the long-time viscosity describes the global phase taking into account the nanodomains, which is approximately 3 times larger than the local viscosity and increases with the DPPC density. We find that the constant short-time viscosity reflects the dynamic equilibrium between the continuous fluid phase and the condensed nanodomains on the molecular scale. Despite the

multistage MSD, the short-time or long-time diffusion coefficient can be described by HPW's hydrodynamic theory separately.

Our results stress the unusual DPDs of the diffusion in DPPC monolayer with heterogeneous structures, which contain valuable information of the diffusion dynamics and nanodomain−microdomain interactions. The temporal evolution of the DPD demonstrates that the interaction between a microdomain and the surrounding nanodomains varies on different time scales. In the early stage, the confinement from nearby nanodomains dominates, which can be described and quantified by the energy barrier theory. In the late stage, the dynamic nature of the nanodomains induces a disturbance of the positions of the nanodomains relative to the microdomain, and the unevenly distributed nanodomains induce a net dipolar repulsive force on the microdomain and cause the double-peaked DPD. We stress that the observed double-peaked DPD is closely related to the negative correlation due to the repulsive force from the confinement, which is in line with the latest theoretical prediction.[68] We unveil the double-peaked DPD as a distinct feature of the "anomalous yet Brownian" behavior in the DPPC monolayer, which differs from previously reported non-Gaussian DPDs in other complex systems that exhibit a central sharp peak or heavy tails.[2,41−44,67] Simulations involving the essential dynamic components, such as those in experiments reproducing the MSD and DPDs, support our explanations of the experimental results. Our work emphasizes the effect of heterogeneous nanostructures in lipid membranes, which enriches the hydrodynamic description of membrane inclusions' diffusion with distinct statistical features. The findings provide physical insights into the anomalous diffusion of membrane inclusions that underpin various biological functions and drug deliveries.[73−76]

MATERIALS AND METHODS

Sample Preparation and Monolayer Formation. All experiments were performed at a room temperature of 20 °C. Dipalmitoylphosphatidylcholine (DPPC) was purchased from Avanti Polar Lipids (Alabaster, AL). To prepare the DPPD solution, the DPPC powder was dissolved in chloroform (Sigma-Aldrich, MO) at a concentration of 1 mg/mL. A fluorescent probe, Texas Red 1,2-dihexadecanoyl-sn-glycero-3-phosphoethanolamine (Texas Red-DHPE; Life Technologies, OR), was doped with the DPPC solution at 99.8/0.2 mol/mol (DPPC/Texas). A glass cell culture dish with an inner diameter of 89 mm and a height of 15 mm was used as a trough to contain the DPPD monolayer. Deionized water (Milli-Q, resistivity 18.2 MΩ cm) was poured into the dish to form a supporting layer with a thickness of ∼1 mm. The DPPC monolayer was formed by spreading the DPPC/chloroform solution with a 5 μL Hamilton microsyringe onto the air−water interface. We tuned the surface density of the monolayer by controlling the volume of the DPPC/chloroform solution dropped on the interface.

Microscopic Observation and Particle Tracking. The diffusion of the microdomains was observed using an inverted fluorescence microscope (IX71, Olympus, Japan) with a 60×/1.2 objective lens. An electron-multiplying charge-coupled device (EMCCD) (Ultra897, Andor, Northern Ireland) captured an image sequence of 4000 consecutive frames with an interval time of 0.05 s and an exposure time of 5 ms. A subimage mode was used to crop raw images (512 × 512 pixels) to be approximately 300 × 300 pixels, with a resolution of 0.26 μm/pixel. Photobleaching of the monolayer did not obviously weaken the contrast of black to white of the captured frames within the observation duration of 200 s. To minimize the surface flow of the monolayer, a Teflon ring (outer diameter 12 mm, inner diameter 6 mm, height 2.5 mm) was placed above the monolayer to make a stable region inside. A cover glass was placed on

the top of the ring to reduce air flow disturbance. Several additional hours elapsed to eliminate the directed surface flow. Only the monolayer inside the ring was observed by microscopy. The diffusions of the microdomains with diameters ranging from approximately 1.5 to 11 μm were measured by the particle tracking technique, the method of which is the same as described in our previous work.[43,44] The details of image processing are provided in Supplementary Note 5 and Figure S5 in the Supporting Information. Our method can determine the displacement of the microdomains with a precision of approximately a half pixel.

Atomic Force Microscope Measurement. Prior to AFM imaging, the DPPC monolayer on the air−water interface was transferred to a freshly cleaved mica surface by vertically elevating the presubmerged mica sheet out of the air−water interface at a rate of 1 mm/min.[36] The transferred DPPC monolayer was scanned by AFM within 2 h upon transfer. An AFM instrument (MFP-3D, Asylum Research Inc., USA) was used to image the topography of the transferred monolayer using tapping mode in air. A silicon cantilever with the spring constant $k \approx 2$ N/m was used. Prior to each measurement, we calibrated the spring constant k of the probe using the thermal power spectral density method.[77] The typical imaging resolution is 512×512 pixels at a scanning rate of 0.5 Hz.

ASSOCIATED CONTENT

Supporting Information

The Supporting Information is available free of charge at https://pubs.acs.org/doi/10.1021/acsnano.2c04089.

> Details of the measurement of the compression isotherm, comparison between the SD model and HPW model, an analysis of the dipolar repulsive force between domains, details of the numerical simulation, and the image processing method (PDF)

AUTHOR INFORMATION

Corresponding Author

Guoqing Hu − *Department of Engineering Mechanics, State Key Laboratory of Fluid Power and Mechatronic Systems, Zhejiang University, Hangzhou 310027, People's Republic of China;* orcid.org/0000-0001-9451-5336; Email: ghu@zju.edu.cn

Authors

Yang Liu − *State Key Laboratory of Nonlinear Mechanics (LNM), Beijing Key Laboratory of Engineered Construction and Mechanobiology, Institute of Mechanics, Chinese Academy of Sciences, Beijing 100190, People's Republic of China; Frontier Scientific Research Centre for Fluidized Mining of Deep Underground Resources, China University of Mining & Technology, Xuzhou 221116, China*

Xu Zheng − *State Key Laboratory of Nonlinear Mechanics (LNM), Beijing Key Laboratory of Engineered Construction and Mechanobiology, Institute of Mechanics, Chinese Academy of Sciences, Beijing 100190, People's Republic of China;* orcid.org/0000-0002-2398-9283

Dongshi Guan − *State Key Laboratory of Nonlinear Mechanics (LNM), Beijing Key Laboratory of Engineered Construction and Mechanobiology, Institute of Mechanics, Chinese Academy of Sciences, Beijing 100190, People's Republic of China;* orcid.org/0000-0002-4433-3662

Xikai Jiang − *State Key Laboratory of Nonlinear Mechanics (LNM), Beijing Key Laboratory of Engineered Construction and Mechanobiology, Institute of Mechanics, Chinese Academy of Sciences, Beijing 100190, People's Republic of China;* orcid.org/0000-0001-5601-8339

Complete contact information is available at:
https://pubs.acs.org/10.1021/acsnano.2c04089

Author Contributions

Y.L. and X.Z. contributed equally to this work.

Notes

The authors declare no competing financial interest.

REFERENCES

(1) Singer, S. J.; Nicolson, G. L. The Fluid Mosaic Model of the Structure of Cell Membranes. *Science* **1972**, *175*, 720−731.

(2) Chen, P.; Huang, Z.; Liang, J.; Cui, T.; Zhang, X.; Miao, B.; Yan, L. T. Diffusion and Directionality of Charged Nanoparticles on Lipid Bilayer Membrane. *ACS Nano* **2016**, *10*, 11541−11547.

(3) Yamamoto, E.; Akimoto, T.; Kalli, A. C.; Yasuoka, K.; Sansom, M. S. Dynamic Interactions between a Membrane Binding Protein and Lipids Induce Fluctuating Diffusivity. *Sci. Adv.* **2017**, *3*, e1601871.

(4) Eggeling, C.; Ringemann, C.; Medda, R.; Schwarzmann, G.; Sandhoff, K.; Polyakova, S.; Belov, V. N.; Hein, B.; von Middendorff, C.; Schönle, A.; Hell, S. W. Direct Observation of the Nanoscale Dynamics of Membrane Lipids in a Living Cell. *Nature* **2009**, *457*, 1159−1162.

(5) Grecco, H. E.; Schmick, M.; Bastiaens, P. I. Signaling from the Living Plasma Membrane. *Cell* **2011**, *144*, 897−909.

(6) Simons, K.; Ikonen, E. Functional Rafts in Cell Membranes. *Nature* **1997**, *387*, 569−572.

(7) Jacobson, K.; Mouritsen, O. G.; Anderson, R. G. Lipid Rafts: at a Crossroad between Cell Biology and Physics. *Nat. Cell Biol.* **2007**, *9*, 7−14.

(8) Mayor, S.; Rao, M. Rafts: Scale-Dependent, Active Lipid Organization at the Cell Surface. *Traffic* **2004**, *5*, 231−240.

(9) Zuo, Y. Y.; Uspal, W.; Wei, T. Airborne Transmission of COVID-19: Aerosol Dispersion, Lung Deposition, and Virus-Receptor Interactions. *ACS Nano* **2020**, *14*, 16502−16524.

(10) Hu, Q.; Bai, X.; Hu, G.; Zuo, Y. Y. Unveiling the Molecular Structure of Pulmonary Surfactant Corona on Nanoparticles. *ACS Nano* **2017**, *11*, 6832−6842.

(11) Guagliardo, R.; Herman, L.; Penders, J.; Zamborlin, A.; De Keersmaecker, H.; Van de Vyver, T.; Verstraeten, S.; Merckx, P.; Mingeot-Leclercq, M. P.; Echaide, M.; Pérez-Gil, J.; Stevens, M.; De Smedt, S.; Raemdonck, K. Surfactant Protein B Promotes Cytosolic SiRNA Delivery by Adopting a Virus-Like Mechanism of Action. *ACS Nano* **2021**, *15*, 8095−8109.

(12) Dowdy, S. F. Overcoming Cellular Barriers for RNA Therapeutics. *Nat. Biotechnol.* **2017**, *35*, 222−229.

(13) Kingston, B.; Lin, Z.; Ouyang, B.; MacMillan, P.; Ngai, J.; Syed, A.; Sindhwani, S.; Chan, W. Specific Endothelial Cells Govern Nanoparticle Entry into Solid Tumors. *ACS Nano* **2021**, *15*, 14080−14094.

(14) Bao, C.; Liu, B.; Li, B.; Chai, J.; Zhang, L.; Jiao, L.; Li, D.; Yu, Z.; Ren, F.; Shi, X. H.; Li, Y. Enhanced Transport of Shape and Rigidity-Tuned α-Lactalbumin Nanotubes Across Intestinal Mucus and Cellular Barriers. *Nano Lett.* **2020**, *20*, 1352−1361.

(15) Engelman, D. M. Membranes Are More Mosaic Than Fluid. *Nature* **2005**, *438*, 578−580.

(16) Lingwood, D.; Simons, K. Lipid Rafts As a Membrane-Organizing Principle. *Science* 2010, 327, 46−50.

(17) Jacobson, K.; Liu, P.; Lagerholm, B. C. The Lateral Organization and Mobility of Plasma Membrane Components. *Cell* 2019, 177, 806−819.

(18) Shi, Z.; Graber, Z. T.; Baumgart, T.; Stone, H. A.; Cohen, A. E. Cell Membranes Resist Flow. *Cell* 2018, 175, 1769−1779.

(19) Yu, Y.; Li, M.; Yu, Y. Tracking Single Molecules in Biomembranes: Is Seeing Always Believing? *ACS Nano* 2019, 13, 10860−10868.

(20) Liao, Y. H.; Lin, C. H.; Cheng, C. Y.; Wong, W. C.; Juo, J. Y.; Hsieh, C. L. Monovalent and Oriented Labeling of Gold Nanoprobes for the High-Resolution Tracking of a Single-Membrane Molecule. *ACS Nano* 2019, 13, 10918−10928.

(21) Jeon, J. H.; Javanainen, M.; Martinez-Seara, H.; Metzler, R.; Vattulainen, I. Protein Crowding in Lipid Bilayers Gives Rise to Non-Gaussian Anomalous Lateral Diffusion of Phospholipids and Proteins. *Phys. Rev. X* 2016, 6, 021006.

(22) Javanainen, M.; Martinez-Seara, H.; Metzler, R.; Vattulainen, I. Diffusion of Integral Membrane Proteins in Protein-Rich Membranes. *J. Phys. Chem. Lett.* 2017, 8, 4308−4313.

(23) Jeon, J. H.; Monne, H. M. S.; Javanainen, M.; Metzler, R. Anomalous Diffusion of Phospholipids and Cholesterols in a Lipid Bilayer and Its Origins. *Phys. Rev. Lett.* 2012, 109, 188103.

(24) Javanainen, M.; Hammaren, H.; Monticelli, L.; Jeon, J. H.; Miettinen, M. S.; Martinez-Seara, H.; Metzler, R.; Vattulainen, I. Anomalous and Normal Diffusion of Proteins and Lipids in Crowded Lipid Membranes. *Faraday Discuss.* 2013, 161, 397−417.

(25) Klingler, J. F.; McConnell, H. M. Brownian Motion and Fluid Mechanics of Lipid Monolayer Domains. *J. Phys. Chem.* 1993, 97, 6096−6100.

(26) Wilke, N.; Vega Mercado, F.; Maggio, B. Rheological Properties of a Two-Phase Lipid Monolayer at the Air/Water Interface: Effect of the Composition of the Mixture. *Langmuir* 2010, 26, 11050−11059.

(27) Cicuta, P.; Keller, S. L.; Veatch, S. L. Diffusion of Liquid Domains in Lipid Bilayer Membranes. *J. Phys. Chem. B* 2007, 111, 3328−3331.

(28) Petrov, E. P.; Petrosyan, R.; Schwille, P. Translational and Rotational Diffusion of Micrometer-Sized Solid Domains in Lipid Membranes. *Soft Matter* 2012, 8, 7552−7555.

(29) Höfling, F.; Franosch, T. Anomalous Transport in the Crowded World of Biological Cells. *Rep. Prog. Phys.* 2013, 76, 046602.

(30) Metzler, R.; Jeon, J. H.; Cherstvy, A. G. Non-Brownian Diffusion in Lipid Membranes: Experiments and Simulations. *Biochim. Biophys. Acta-Biomembranes.* 2016, 1858, 2451−2467.

(31) Liu, C.; Elvati, P.; Majumder, S.; Wang, Y.; Liu, A.; Violi, A. Predicting the Time of Entry of Nanoparticles in Lipid Membranes. *ACS Nano* 2019, 13, 10221−10232.

(32) Raghunandan, A.; Hirsa, A.; Underhill, P.; Lopez, J. M. Predicting Steady Shear Rheology of Condensed-Phase Monomolecular Films at the Air-Water Interface. *Phys. Rev. Lett.* 2018, 121, 164502.

(33) Saffman, P. G.; Delbrück, M. Brownian Motion in Biological Membranes. *Proc. Natl. Acad. Sci. U.S.A.* 1975, 72, 3111−3113.

(34) Hughes, B. D.; Pailthorpe, B. A.; White, L. R. The Translational and Rotational Drag on a Cylinder Moving in a Membrane. *J. Fluid. Mech.* 1981, 110, 349−372.

(35) Shkulipa, S. A.; den Otter, W. K.; Briels, W. J. Surface Viscosity, Diffusion, and Intermonolayer Friction: Simulating Sheared Amphiphilic Bilayers. *Biophys. J.* 2005, 89, 823−829.

(36) Zuo, Y. Y.; Chen, R.; Wang, X.; Yang, J.; Policova, Z.; Neumann, A. W. Phase Transitions in Dipalmitoylphosphatidylcholine Monolayers. *Langmuir* 2016, 32, 8501−8506.

(37) Cruz, A.; Vázquez, L.; Vélez, M.; Pérez-Gil, J. Influence of a Fluorescent Probe on the Nanostructure of Phospholipid Membranes: Dipalmitoylphosphatidylcholine Interfacial Monolayers. *Langmuir* 2005, 21, 5349−5355.

(38) Weigel, A. V.; Simon, B.; Tamkun, M. M.; Krapf, D. Ergodic and Nonergodic Processes Coexist in the Plasma Membrane As Observed by Single-Molecule Tracking. *Proc. Natl. Acad. Sci. U.S.A.* 2011, 108, 6438−6443.

(39) Manzo, C.; Torreno-Pina, J.; Massignan, P.; Lapeyre, G.; Lewenstein, M.; Parajo, M. Weak Ergodicity Breaking of Receptor Motion in Living Cells Stemming from Random Diffusivity. *Phys. Rev. X* 2015, 5, 011021.

(40) Vicidomini, G.; Ta, H.; Honigmann, A.; Mueller, V.; Clausen, M. P.; Waithe, D.; Galiani, S.; Sezgin, E.; Diaspro, A.; Hell, S. W.; Eggeling, C. STED-FLCS: an Advanced Tool to Reveal Spatiotemporal Heterogeneity of Molecular Membrane Dynamics. *Nano Lett.* 2015, 15, 5912−5918.

(41) He, W.; Song, H.; Su, Y.; Geng, L.; Ackerson, B. J.; Peng, H. B.; Tong, P. Dynamic Heterogeneity and Non-Gaussian Statistics for Acetylcholine Receptors on Live Cell Membrane. *Nat. Commun.* 2016, 7, 11701.

(42) Wang, B.; Anthony, S. M.; Bae, S. C.; Granick, S. Anomalous Yet Brownian. *Proc. Natl. Acad. Sci. U.S.A.* 2009, 106, 15160−15164.

(43) Xue, C.; Zheng, X.; Chen, K.; Tian, Y.; Hu, G. Probing Non-Gaussianity in Confined Diffusion of Nanoparticles. *J. Phys. Chem. Lett.* 2016, 7, 514−519.

(44) Xue, C.; Shi, X.; Zheng, X.; Tian, Y.; Hu, G. Diffusion of Nanoparticles with Activated Hopping in Crowded Polymer Solutions. *Nano Lett.* 2020, 20, 3895−3904.

(45) Xu, L.; Yang, Y.; Zuo, Y. Y. Atomic Force Microscopy Imaging of Adsorbed Pulmonary Surfactant Films. *Biophys. J.* 2020, 119, 756−766.

(46) Roke, S.; Schins, J.; Müller, M.; Bonn, M. Vibrational Spectroscopic Investigation of the Phase Diagram of a Biomimetic Lipid Monolayer. *Phys. Rev. Lett.* 2003, 90, 128101.

(47) Dadashvand, N.; Williams, L. A.; Othon, C. M. Heterogeneous Rotational Diffusion of a Fluorescent Probe in Lipid Monolayers. *Struct. Dyn.* 2014, 1, 054701.

(48) Kim, K.; Choi, S. Q.; Zasadzinski, J. A.; Squires, T. M. Interfacial Microrheology of DPPC Monolayers at the Air-Water Interface. *Soft Matter* 2011, 7, 7782−7789.

(49) McConlogue, C. W.; Vanderlick, T. K. A Close Look at Domain Formation in DPPC Monolayers. *Langmuir* 1997, 13, 7158−7164.

(50) Kaganer, V. M.; Möhwald, H.; Dutta, P. Structure and Phase Transitions in Langmuir Monolayers. *Rev. Mod. Phys.* 1999, 71, 779−819.

(51) Rufeil-Fiori, E.; Wilke, N.; Banchio, A. J. Dipolar Interactions between Domains in Lipid Monolayers at the Air-Water Interface. *Soft Matter* 2016, 12, 4769−4777.

(52) Ochab-Marcinek, A.; Hołyst, R. Scale-Dependent Diffusion of Spheres in Solutions of Flexible and Rigid Polymers: Mean Square Displacement and Autocorrelation Function for FCS and DLS Measurements. *Soft Matter* 2011, 7, 7366−7374.

(53) Yu, M.; Song, W.; Tian, F.; Dai, Z.; Zhu, Q.; Ahmad, E.; Guo, S.; Zhu, C.; Zhong, H.; Yuan, Y.; Zhang, T.; Yi, X.; Shi, X.; Gan, Y.; Gao, H. Temperature- and Rigidity-Mediated Rapid Transport of Lipid Nanovesicles in Hydrogels. *Proc. Natl. Acad. Sci. U.S.A.* 2019, 116, 5362−5369.

(54) Ma, X. G.; Lai, P. Y.; Tong, P. Colloidal Diffusion Over a Periodic Energy Landscape. *Soft Matter* 2013, 9, 8826−8836.

(55) Peng, Y.; Chen, W.; Fischer, T. M.; Weitz, D. A.; Tong, P. Short-Time Self-diffusion of Nearly Hard Spheres at an Oil−Water Interface. *J. Fluid. Mech.* 2009, 618, 243−261.

(56) Gupta, S.; De Mel, J. U.; Perera, R. M.; Zolnierczuk, P.; Bleuel, M.; Faraone, A.; Schneider, G. J. Dynamics of Phospholipid Membranes Beyond Thermal Undulations. *J. Phys. Chem. Lett.* 2018, 9, 2956−2960.

(57) Lampo, T. J.; Stylianidou, S.; Backlund, M. P.; Wiggins, P. A.; Spakowitz, A. J. Cytoplasmic RNA-Protein Particles Exhibit Non-Gaussian Subdiffusive Behavior. *Biophys. J.* 2017, 112, 532−542.

(58) Harland, C. W.; Bradley, W. J.; Parthasarathy, R. Phospholipid Bilayers Are Viscoelastic. *Proc. Natl. Acad. Sci. U.S.A.* 2010, 107, 19146−19150.

(59) Petrov, E. P.; Schwille, P. Translational Diffusion in Lipid Membranes Beyond the Saffman Delbrück Approximation. *Biophys. J.* **2008**, *94*, L41−L43.

(60) Kalathi, J. T.; Yamamoto, U.; Schweizer, K. S.; Grest, G. S.; Kumar, S. K. Nanoparticle Diffusion in Polymer Nanocomposites. *Phys. Rev. Lett.* **2014**, *112*, 108301.

(61) Su, Y.; Ma, X. G.; Lai, P. Y.; Tong, P. Colloidal Diffusion Over a Quenched Two-Dimensional Random Potential. *Soft Matter* **2017**, *13*, 4773−4785.

(62) Hänggi, P.; Talkner, P.; Borkovec, M. Reaction-Rate Theory: Fifty Years after Kramers. *Rev. Mod. Phys.* **1990**, *62*, 251−341.

(63) Schweizer, K. S.; Saltzman, E. J. Entropic Barriers, Activated Hopping, and the Glass Transition in Colloidal Suspensions. *J. Chem. Phys.* **2003**, *119*, 1181−1196.

(64) Saltzman, E. J.; Schweizer, K. S. Activated Hopping and Dynamical Fluctuation Effects in Hard Sphere Suspensions and Fluids. *J. Chem. Phys.* **2006**, *125*, 044509.

(65) Ghosh, S. K.; Cherstvy, A. G.; Metzler, R. Non-Universal Tracer Diffusion in Crowded Media of Non-Inert Obstacles. *Phys. Chem. Chem. Phys.* **2015**, *17*, 1847−1858.

(66) Zheng, X.; Ten Hagen, B.; Kaiser, A.; Wu, M.; Cui, H. H.; Silber-Li, Z. H.; Löwen, H. Non-Gaussian Statistics for the Motion of Self-Propelled Janus Particles: Experiment versus Theory. *Phys. Rev. E* **2013**, *88*, 032304.

(67) Wang, B.; Kuo, J.; Bae, S. C.; Granick, S. When Brownian Diffusion Is Not Gaussian. *Nat. Mater.* **2012**, *11*, 481−485.

(68) Vojta, T.; Skinner, S.; Metzler, R. Probability Density of the Fractional Langevin Equation with Reflecting Walls. *Phys. Rev. E* **2019**, *100*, 042142.

(69) Wang, W.; Seno, F.; Sokolov, I. M.; Chechkin, A. V.; Metzler, R. Unexpected Crossovers in Correlated Random-Diffusivity Processes. *New J. Phys.* **2020**, *22*, 083041.

(70) Höfling, F.; Franosch, T.; Frey, E. Localization Transition of the Three-Dimensional Lorentz Model and Continuum Percolation. *Phys. Rev. Lett.* **2006**, *96*, 165901.

(71) Chakraborty, I.; Roichman, Y. Disorder-Induced Fickian, Yet Non-Gaussian Diffusion in Heterogeneous Media. *Phys. Rev. Res.* **2020**, *2*, 022020.

(72) Goulian, M. Inclusions in Membranes. *Curr. Opin. Colloid Interface Sci.* **1996**, *1*, 358−361.

(73) Song, X.; Feng, L.; Liang, C.; Yang, K.; Liu, Z. Ultrasound Triggered Tumor Oxygenation with Oxygen-Shuttle Nanoperfluorocarbon to Overcome Hypoxia-Associated Resistance in Cancer Therapies. *Nano Lett.* **2016**, *16*, 6145−6153.

(74) Shi, A.; Claridge, S. A. Lipids: An Atomic Toolkit for the Endless Frontier. *ACS Nano* **2021**, *15*, 15429−15445.

(75) Bao, W.; Tian, F.; Lyu, C.; Liu, B.; Li, B.; Zhang, L.; Liu, X.; Li, F.; Li, D.; Gao, X.; Wang, S.; Wei, W.; Shi, X.; Li, Y. Experimental and Theoretical Explorations of Nanocarriers' Multistep Delivery Performance for Rational Design and Anticancer Prediction. *Sci. Adv.* **2021**, *7*, eaba2458.

(76) Pan, Q.; Sun, D.; Xue, J. F.; Hao, J.; Zhao, H.; Lin, X.; Yu, L.; He, Y. Real-Time Study of Protein Phase Separation with Spatiotemporal Analysis of Single-Nanoparticle Trajectories. *ACS Nano* **2021**, *15*, 539−549.

(77) Guan, D.; Hang, Z. H.; Marcet, Z.; Liu, H.; Kravchenko, I.; Chan, C. T.; Chan, H. B.; Tong, P. Direct Measurement of Optical Force Induced by Near-Field Plasmonic Cavity Using Dynamic Mode AFM. *Sci. Rep.* **2015**, *5*, 16216.